Microelectronic Junctions in Arsenian Pyrite Due to Impurity and Mixed Sulphide Heterogeneity

REVISION 3

Jamie S Laird [1,2,3], Colin M MacRae [5], Angela Halfpenny [4], Ross Large [2] and Chris G Ryan [1,2,3]

[1] CSIRO, Earth Science and Resource Engineering, Normanby Road, Clayton VIC, Australia

[2] Centre of Excellence in Ore Deposits (CODES), University of Tasmania, Hobart, Australia

[3] School of Physics, University of Melbourne, Melbourne VIC, Australia

[4] CSIRO, Earth Science and Resource Engineering, ARRC Kensington, Perth WA, Australia

[5] CSIRO, Processing Science and Engineering, Normanby Road, Clayton VIC, Australia

Abstract:

Impurities and crystal defects within the semiconducting bulk of a metal sulfide introduce energy levels within the forbidden bandgap. These levels in turn control semiconducting type and local electrical properties within single and multi-phased sulfide assemblages. Heterogeneity in sulfide semiconductivity linked to these impurities can lead to *p-n* micro-junction formation and potential distributions near the surface that may alter redox reactivity. Secondary gold ore genesis via a micro-galvanic effect related to heterogeneity has in the past been hypothetically linked to such micro-junctions. Understanding these regions and their interaction with weathering fluids in the regolith for example requires large scale imaging of potential distributions associated with near-surface micro-junctions and correlation with the responsible elemental distributions. Here we investigate the existence of micro-electronic junctions in a mixed sulfide assemblage using Scanning Laser Beam Induced Current (LBIC) and correlate them with pyrite-chalcopyrite interfaces mapped using combined Energy Dispersive Spectroscopy (EDS) and Wavelength Dispersive Spectroscopy (WDS) on an electron hyper-probe. Junctions in a natural assemblage are positively identified for the first time.

Keywords: pyrite, heterogeneity, semiconductors, electrical properties, micro-junction, heterojunction, chalcopyrite, mixed sulfides, laser beam induced current, elemental mapping, metal ore genesis, electrochemical

INTRODUCTION

Semiconducting metal sulfides such as pyrite, galena and chalcopyrite all possess unique electrical properties that depend not only on crystal structure but also heterogeneity in minor and trace level impurities (Pridmore and Shuey 1976; Abraitis et al. 2004). These impurities introduce discrete energy levels into the forbidden bandgap (global minima in energy difference between the conduction band (CB) and valence band (VB)) some of which radically alter electrical properties (Sze 1985). The resultant electrical properties of the bulk and surface of pyrite are intimately linked to impurity and defect concentrations and importantly, their textural fabrics (Pridmore and Shuey 1975). Broken bonds and low co-ordination surface sites due to conchoidal fracture for example can lead to band-gap narrowing (BGN), inversion layers (Bronold et al. 1994) and heterogeneous electrical properties across the surface (Chandra and Gerson 2010). Band structure constants including the density of states and position of the conduction and valence band edges and their energy or band-gap can all vary within a single sulfide phase. On top of this variation are the shifting electron and hole Fermi levels due to ionized impurities. Absolute band positions close to the bandgap minimum for a range of common metal sulfides are given in **Figure 1**(A) relative to vacuum and SHE.

In sulfides, an excess metal cation corresponds to a sulphur deficiency resulting in an electron free to conduct if its level is within a lattice thermal energy k_BT away from the CB edge (~26 meV at room temperature). This is termed an *n*-type or donor level with the opposite due to an acceptor level close to the VB edge, being a *p*-type or acceptor level (Sze 1985). Extrinsically *n* or *p*-doped materials conduct charge via their majority carrier i.e. electrons or holes, respectively (Sze 1985). In nature, the types of impurities present and their heterogeneities are largely determined by the sulfide formation sequence, subsequent diagenesis as well as any metamorphic activity and weathering. Pyrite being the most abundant sulfide appears in a wide range of geological settings including hydrothermal, igneous and sedimentary. Each setting in turn influences the overall habit, impurity levels and their heterogeneity (Large et al. 2009). For example, large impurity gradients or even elemental zonation are often associated with hydrothermally altered rims. Zoned pyrites are common in many Carlin and Bendigo-type gold deposits and the subject of numerous studies including those by Large et al. (2009), Fleet et al. (1993,1997), Craig et al. (1998) and

Den Besten et al. (1999). Importantly, one can easily construe regions within sulfide ores where *p* and *n*-type materials butt one another forming *p-n* micro-junctions. Indeed, impurity segregation in zoned pyrites resulting in neighboring *p* and *n* regions have been noted but not verified by Vaughan et al. (1991) and Marion et al. (1991). Micro-junctions can also form at mixed phase boundaries due to offsets in band-structure transitioning from one phase to another as shown in **Figure 1**(A). Consider for example the chalcopyrite-pyrite (cp-py) heterojunction displayed in **Figure 1**(B). At thermal equilibrium, the Fermi level E_f^p in arsenian pyrite and E_f^n in the chalcopyrite must align causing energy band-bending at the interface and an electric-field which points from cp (*n*) to py (*p*) as in a single-phase micro-junction. The effect of the *E*-field is to limit the diffusion of majority carriers across the junction resulting in a potential difference or open-circuit voltage OCV (electrochemical rest potential on the SHE scale). In reality, the Fermi level close to the surface of pyrite appears pinned close to mid-gap due to a large number of defects and surface states which reduces the OCV to less than 200 mV (Maddox et al. 1998 and Buker et al. 1992). Importantly from a geochemical perspective this OCV may still provide a driving force for diagenetic chemical change by shifting *Eh* for a particular rock-fluid reaction. For example, both observation and calculations based on Density Functional Theory (DFT) suggests As, Ni and Co substitution and their heterogeneity results in higher oxidation rates during pyrite flotation (Abraitis et al. 2004; Savage et al. 2008; Li et al. 2011). These effects are not to be confused with the fact that a low concentration of vanishingly soluble impurity atoms also reduces mineral stability providing a thermodynamic reason for higher reactivity.

A complex mineral assemblage can therefore be viewed as a three-dimensional circuit (Abraitis et al. 2004) with certain textural fabrics in *n* and *p* regions controlling static potentials throughout the assemblage. If pushed off equilibrium by an alteration due to electrochemical activity at a surface for example, the overall circuit will control the rate of flow of free carriers as well as their paths. Any *excess* charge will seek a return electrical ground by the shortest resistance and/or recombine with its conjugate carrier (neutralize). It is not hard then to envisage an assemblage of mixed sulfides as an electrical circuit at equilibrium with micro to macro scale variations in potential and by corollary, field strengths. Surface potential variations associated with micro-junctions shift the local redox balance and in theory protect or enhance abiotic and/or biotic oxidative attack. Depending on location within the electrical network, a reaction on one surface might lead to action somewhere remote (Becker et al. 2001). Taking this argument a step further, one can envisage mineral-fluid scenarios in which junctions exposed to fluids with the right pH act as galvanic cells leading to precious metal trapping as postulated by Moller and Kersten (1994) and Meyer et al. (1999) for the case of visible gold.

To date however, no successful attempts to isolate and measure the existence of micro-junctions have been made. The primary interest in this work is proving their existence whether related to dopant heterogeneity within a single phase or an interface between mixed sulfides. To do so we use a Scanning Laser Microscope and the Remote Laser Beam Induced Current (LBIC) (Bajaj et al. 1993) method to map internally generated electric-field distributions close to the surface of a sulfide assemblage comprising a black shale host with large 0.5-2 mm euhedral to subhedral zoned arsenian pyrite from the Otago-Schist, New Zealand. Internally generated electric-fields have for the first time been correlated with impurity and mixed sulfide heterogeneity measured afterwards using element mapping on an electron probe. Evidence is shown for their existence, in this instance those with the best signal to noise ratio are linked to mixed sulfide phase heterojunctions. Evidence pointing to junctions related to As-Ni variation was obtained although a direct correlation was not possible due to the sheer complexity in both the elemental zoning and LBIC maps.

BACKGROUND

Impurity heterogeneity, structural imperfections and small changes in stoichiometry leading to variation in electrical properties are typically measured via their influence on resistivity (Abraitis et al. 2004; Savage et al. 2008; Lehner et al. 2006). Illustrating the scale of spread in resistivity, an early compilation by Pridmore et al. (1976) on natural pyrite found *n*-type samples to span four orders of magnitude. *P*-type samples on the other hand, generally had higher resistivities but with a smaller spread. Later, Doyle et al. (1996) made similar measurements but observed a narrower spread in resistivity for *n*-type samples than for *p*-type samples. According to Fleet et al. (1993), arsenian pyrite predominantly forms in low temperature hydrothermal environments. Sedimentary and epithermal pyrite tends to be *p*-type with Fe/S ratios less than 2 whereas those formed under hydrothermal settings are mostly *n*-type with Fe/S ratios greater than 2 (Pridmore and Shuey 1976). However, pinning down electrical properties in zoned sulfides for example is obviously prone to large errors since resistivity typically being a macroscopic measurement ultimately averages over microscopic variations. In highly heterogeneous sulfides such as zoned pyrites with alternating *n* and *p* regions an *effective* assignment is therefore highly erroneous (Pridmore and Shuey 1976).

Pyrite Band-structure

Pyrite (FeS_2) has a rock salt or face centered cubic structure with Fe^{2+} ions occupying the cationic sites and S_2^{2-} dimers, the anionic sites. Pyrite belongs to the $T_h^6 - Pa3$ group and is diamagnetic (Abraitis et al. 2004). Electro-reflectance (EER) measurements by Huang et al. (1993) have confirmed it has an indirect bandgap E_g from the bottom of the conduction band (S 3p σ^* anti-bonding levels) to the Fe 3d levels of the valence band as depicted in Figure 2. Theoretical band structure calculations as well as electrical and optical measurements give an E_g of 0.80-0.93 eV (Pridmore and Shuey 1974, 1975; Ennaoui et al. 1986,1993; Schiek et al. 1990). A large spread in bandgap values for both natural and synthetic samples appears related to stoichiometry, microstructure and the incorporation of high levels of impurities (Abraitis et al. 2004).

Summary of Impurities and Electrical Influence

Common impurities known to alter the electrical properties of natural sulfides are As, Ni, Co and Cu (Pridmore and Shuey 1975, 1976; Abraitis et al. 2004; Savage et al. 2008; Lehner et al. 2007). That is not to say other metallic impurities fail to alter electrical properties, but that exhaustive measurements on their influence are yet to be done. A summary of impurities and their relative location within the pyrite bandgap are shown in Figure 2. A red circle indicates hole flow, which is opposite to that of an electron. Importantly, the effective semiconductor type at a given location depends on the sum of all donor-and acceptor-like states. The dominant concentration will generally but *not* always determine electrical behavior (Sze 1985). In arsenian $FeAs_xS_{2-x}$ and arsenopyrite $Fe(S,As)_2$ for example, As substitutes for S (As_S) and is almost always *p*-type as a result (Lehner et al 2006). Cobalt and Cu substitution with Fe (Co_{Fe} and Cu_{Fe}) are both partially ionized at room temperature resulting in *n*-type behavior. Despite the overall semiconductor type, resistivity is dominated by Co if present (Savage et al. 2008; Lehner et al. 2007).

Studies on synthetic pyrite by Ho et al. (2006) postulate that Ni^{2+} forms a dopant-like level close to the CB edge where it would contribute to *n*-type conductivity. However, previous work by Lehner et al. (2006, 2007) and Savage et al. (2008) concluded Ni to have no significant influence on carrier concentration. Even earlier work by Chandler and Bene (1974) and Yu et al. (1992) both point to its substitution with Fe (Ni_{Fe}) generating a deep level defect band that must be incompletely ionized at room temperature. More recent Hall measurements versus temperature by Lehner et al. (2012) confirm Ni_{Fe} results in deep-levels at 0.37 eV and 0.42 eV below the CB edge. Although these levels will not contribute to extrinsic conductivity, they may trap carriers from either band and contribute to generation-recombination (GR) based leakage currents in a micro-junction (Sze 1985) which decreases the OCV and short-circuit photocurrent measured by LBIC (Laird et al. 2012).

Although not an impurity, the defect level denoted S_v is theoretically an acceptor defect close to the VB edge and should result in *p*-type doping (Savage et al. 2007; Ho et al. 2006). However, measurements by Ares et al. (2004) on thin films of pyrite suggest it forms a level close to the CB. Ares et al. also note the generation of a defect band at 0.11 eV above the VB due to Fe vacancies, Fe_v. Such a level would not contribute holes to the VB since it is too far from the band edge at room temperature. This combined with the inability to directly measure their concentration means their exclusion from calculations to follow. These defect levels and issues related to ultra-high doping levels in natural minerals are the largest source of error in determining the overall semiconducting behavior of the bulk.

Laser Beam Induced Current Microscopy

The mapping of semiconductor micro-junctions using Laser Beam Induced Current (LBIC) and its various incarnations has been used extensively throughout microelectronics research; from qualifying HgGdTe infra-red detectors (Bajaj 1993; Redfern 2006) through to simulating cosmic rays interactions with space-based microelectronics (Buchner 1988). Only recently however, has its so called remote mode been used for the analysis of natural minerals where the massive noise floor associated with impure material far outweighs any generated signal (Laird et al. 2012). A large advantage of LBIC over competing techniques like Electron Beam Induced Current (EBIC) (Leamy 1982) or Ion Beam Induced Current (IBIC) (Breese and King et al. 1992) is that the intensity of the beam can be readily modulated which allows the use of sophisticated noise suppression methods using Lock-In Amplifiers (LIA) (Laird et al. 2012). Imaging techniques based on ionizing particles also charge oxidation products on the surface leading to distortion in any underlying *E*-fields. Furthermore, the non-invasiveness of photons is important in preserving local electrical properties sensitive to particle beam induced damage.

The basis of the remote LBIC method for natural minerals is now described. Consider the *p*-*n* junction formed between As and Co rich pyrite illustrated in **Figure 3**. Ideally an electric field of width w_j is established laterally from $-x_n$to $+-x_p$ (Sze 1985). The lateral extent of the field depends on doping levels on either side of the junction i.e. the As and Co concentrations. A closer view showing the electric-field distribution, assumed to be uniform, is given in the bottom of the figure. In remote LBIC microscopy, an intensity-modulated diffraction-limited laser spot is scanned in one direction between two ohmic probes situated on either side and well away from the junction of interest as shown in **Figure 3** (Redfern et al. 2006). The wavelength of the laser is carefully chosen to induce band-to-band transitions generating free electrons and holes at the surface of the metal sulfide. The wavelength should be long enough to pass through any surface oxidation products if not already polished or etched off. For all sulfides except sphaelarite, visible wavelengths above UV are suited and spots sizes around 1μm are routinely used.

Under low-injection conditions, the electron-hole pair plasma generated by photon absorption experiences an electrostatic force due to the full *E*-field in the junction. These free carriers drift along the field lines causing minority carrier flows which can be measured as either a short circuit current (photocurrent) or an open circuit photovoltage depending on external circuitry (Laird et al. 2012). The form of the signal is discussed later. Carriers separated by the field “seek to recombine via a return current distributed over all current paths including two ohmic contacts held near ground” (Redfern 2004). Minority carriers generated within several diffusion lengths $L_{n,p}$ from the junction also result in a photocurrent, albeit much smaller. However, the minority carrier lifetimes and diffusion lengths in natural minerals $L_{n,p}$ are likely sub-micron due to the large number of impurities and defects. An LBIC signal above background corresponds to a location containing a junction. Zero photocurrent is collected in neutral regions where the field is zero. Scanning the laser spot from left to right across the junction leads to the bipolar current profile shown in the figure. The first edge encountered at $-x_p$ results in a positive current due to majority carriers arriving from the right, whilst the second at $+x_n$ contributes a negative current due to the same process but in the opposite direction. The region in between is typically linear for a uniform *E*-field profile (Bajaj 1993; Fynn 1995) but also depends strongly on doping levels (Niu et al. 1976, 1977). With $L_{n,p} < 1\mu m$ these bipolar signatures are expected to be extremely sharp in sulfide samples. The non-uniform LBIC profile between junction extremities is a major disadvantage of the method. Translation to a real electric field distribution requires a unique solution to the equations governing carrier behavior in semiconductors coupled with electromagnetism, which is difficult to model even with well-known elements (Fynn et al. 1995). An absolute quantification of the electric-field in natural minerals is an intractable problem until sufficiently complex inverse models are established (Redfern and Smith et al. 2006; Laird et al. 2012). According to Laird et al. (2012) however, despite limitations of the method it is still nevertheless valuable in qualifying the existence of junctions and for extracting relative field strengths even in the presence of an irregular weathered surface (Laird et al. 2012). Here we simply aim to map a photocurrent that is indicative of an *E*-field and use relative changes in photocurrent to map junction locations. Tributsch et al. (2003) have observed photo-electrochemical currents in pyrite albeit with an experimental configuration quite different to that used here. In that case the photo-electrochemical properties of the surface were mapped with a much poorer spatial resolution whilst the mineral was immersed in a liquid. The junction measured was related to the Helmholtz layer at the liquid-sulfide interface, not a *p-n* micro-junction.

Materials and Methods

Mineral Preparation for LBIC

As noted earlier, variation in the potential throughout an assemblage can be represented by a three dimensional circuit composed of complex impedances with unknown interdependencies (Savage et al. 2008; Laird et al. 2012). Unraveling the existence of micro-junctions requires some simplification; most especially a 3-D to 2-D circuit transformation by thin-sectioning to a width much less than the smallest granularity under study (Laird et al. 2012) or by using samples with sparse grains as in this case. This ensures the section thickness will mostly contain single grains. Thin sections also reduce the likelihood of underlying shorts. Any short with a resistance comparable to R_n and R_p again circulates current in loops not sampled by external instrumentation. It goes without saying that any minerals should be prepared so as to minimize the chance of shorting at the surface via metal inclusions or conducting coats applied for electron or ion probing of elemental concentrations for example. A null field measurement does not prove the absence of a junction. Assuming a successful 3-D to 2-D planarization, a simple lateral junction between say As and Co rich pyrite has the equivalent circuit of **Figure 3**.

For this sample the assemblage rock was fixed into a 1” epoxy stub and sectioned with a diamond saw to expose several pyrite grains. It was then subjected to several polishing stages with the final being a sub-micron finish with a fine diamond paste. For EBSD measurements not discussed here an ion-beam system was also used to clean the surface. Carbon coating for quantitative elemental mapping was done after LBIC measurements using an evaporative coater. The coat was approximately 10 nm thick.

LBIC Measurements

A major caveat of imaging natural minerals is that regardless of how successfully one manages to make a 3D to 2D transition for the section under study, the simple enormity of defects and impurities in most natural sulfides results in a junction dynamic resistance R_j many orders of magnitude smaller than in modern optoelectronic devices for example (Laird et al. 2012) i.e. an extremely large DC leakage current. Most of the leakage current responsible for low R_j in natural sulfides is due to the GR currents mentioned early; in this arsenian pyrite Ni impurities would be predominantly responsible in combination with an undetected vacancy and interstitial defect populations (S_v and Fe_V). This poses a serious issue for the LBIC sensitivity since poor isolation across the junctions means a large fraction of the generated current simply re-circulates across the junction to recombine rather than pass through the external probes via some series resistance R_n and R_p as shown in the Figure i.e. the measure photocurrent is that generated minus the dark current which flows in the opposite direction. The measured photocurrent $P(f_m)$ is not only much reduced but increased shot noise associated with junction leakage ensures LBIC signals are buried within noise. Making highly sensitive measurements therefore makes use of the fact that in frequency space a noise spectrum is typically broad compared to an LBIC signal generated with a single modulation frequency, f_m. Sophisticated circuitry in a LIA is able to use this fact to highly discriminate signal from noise as well as measure a phase change ϕ between the stimulus and observed photocurrent or open circuit photovoltage. For the remote-LBIC presented here, the LIA measures a short-circuit photocurrent phasor at each pixel given by:

$$P(x,y,f_m) = X(x,y,f_m) + iY(x,y,f_m) \qquad (1)$$

where X and Y are the real and imaginary components of the photocurrent vector. The representation as a complex number arises from the phase introduced by the LBIC AC current generation process together with the effect of the complex impedance between the laser probe and collecting electrodes i.e. the influence of the effective circuit filter on the AC signal amplitude and phase. The magnitude of the phasor is simply:

$$|P|(x,y,f_m) = \sqrt{X^2 + Y^2} \qquad (2)$$

As shown later, laser probe wavelength can be selected to probe down to some depth d, which for metal sulfides is less than a micron or so. This not only simplifies interpretation but also increases the chance that junctions will be lateral rather than vertical, and hence directly comparable to 2D elemental maps.

METHODS

Elemental Mapping: A field emission electron microprobe (Macrae et al. 2005) was used to collect BSE, EDS and WD images over the dual grain pyrite complex. The probe acceleration voltage was set at 20 kV and a beam current of 100 nA was scanned over the sample with a pixel dwell-time of 70 ms. WDS windows were set for Fe and electrically important impurities including As, Ni and Co. Cu and other elements such as Si, Ca and P were observed on the EDX channel. Although concentration levels down to parts per trillion can determine conductivity type in pure semiconductors, natural sulfides are “dirty” by comparison possessing large impurity concentrations. The sensitivity of WD and EDS imaging is well able to cater with the effective dopant levels in this sample since As at a few wt% dominates both grains. In fact WDS is well able to map all of the impurity levels studied in pyrite. A more sensitive elemental mapping method like Particle Induced X-ray Emission (PIXE) might be required when *all* impurity concentrations are less than around 100 ppm. This is not the case here.

Micro-junction Mapping:

Mapping the internal electric fields related to micro-junctions uses the remote-LBIC system detailed elsewhere (Laird et al. 2012). Only a brief summary is given here starting with the optical source. A Coherent Cube 633 nm (1.96eV) free-space laser mounted on a breadboard situated above the microscope feeds into the microscope and focused to a 1-2μm spot using ×80 objective. The mineral itself is mounted on a Newport XY stage and scanned in increments down to 1 µm. Two micromanipulator probes mounted on the stages make ohmic contact at the two widest extremes. Whilst one of these is grounded, the other connects directly to a Lock-In-Amplifier (SRS-830) with a fixed gain of 10^6 or 10^8 V/A. A PC collects various parameters including X, Y, ϕ, and $|P|$ as a function of laser spot co-ordinates. The entire system resides in a dark faraday cage to ensure zero interference from background EM radiation and external light.

RESULTS

Element Mapping

Pyritic shale with large euhedral grains of arsenian pyrite sourced from Otago, N.Z. were chosen for this study due to their relative depletion in ore forming metals (any large ore presence *can* interfere with the sensitivity of *E*-field measurements by shorting junctions). The conglomerate mineral analyzed is predominantly a dual euhedral grain separated by a high-angle grain boundary (HAGB) from B to B' as illustrated in the Back Scattered Electron (BSE) map shown in Figure 4. EBSD data not shown here confirmed the orientation of the two grains.

The rest of the figure summarizes the most important results of the analysis. Firstly, the pyrite grains are embedded in heavily altered quartz surrounded by Al-rich black shale (see online resources for maps). The pyrite grains contain numerous inclusions of both gangue carbonates and mixed sulfides including chalcopyrite (cp) and sphaelarite (sp). Judging by morphology in the BSE image, cubic growth in pyrite hints that unimpeded stable growth conditions early on in paragenesis lead to independent euhedral grains which ultimately collided causing the HAGB (B-B'). Numerous inclusions seen along the grain boundary are mostly carbonates (see online resources) or chalcopyrite as seen in Figure 4. Cu appears to be largely absent from both grains except within the cp inclusions marked by the circles R_1 to R_4. Within the pyrite, dominant impurities that alter semiconductor type are As, Co and Ni (to less of an extent). Both As and Ni are heavily altered and even zoned in parts whereas Co tends to remain close to crystal rims except one large square-like distribution in the top grain. All relevant concentrations are later used to estimate extrinsic doping.

Micro-junction Mapping

LBIC data was collected with the 1.96eV laser at 20 μm steps over a 2mm×2mm square encompassing both large grains as well as several of the smaller satellite euhedral cubes. The total LBIC data array is composed of phasor image data taken as a function of laser intensity modulation from 20 to 500 Hz. To achieve a suitable Signal-to-Noise ratio relatively high laser powers of up to 40mW were used with pixel dwell times of 1.5 s. Considerable heat is dumped into the sample. The resultant X,Y and $|P|$ maps versus modulation frequency are given in **Figure 5**. Note that LBIC images were collected with an approximate 20° rotation with respect to elemental maps.

DISCUSSION

Map of Effective Doping

Predictive estimates of electrical activity in arsenian pyrite require quantitative ionization models for impurity levels that do not exist for metal sulfides. For brevity impurity ionization in these samples is discussed in the supplementary material. The main point derived is that an estimate of effective doping based on impurity concentrations can be made if we assume the main dopant populations are substitutional and near-completely ionized at room temperature. These assumptions are reasonable for As and Co since they are known to be close to their respective band edges but not for Ni. Since its levels are more than $10k_BT$ away from either band edge it will remain completely filled with zero net charge in neutral material. Cu plays a minor role throughout the py and is not included in calculating an effective doping map $D(x,y)$ which under these assumptions is simply the difference between the As and Co concentrations as shown in Figure 4.

Although there is large variation in $D\ (x,y)$, its value never goes negative predicting *p*-type behavior across both pyrite grains. However, junctions with weaker field strengths can also form due to variation in band-structure due to band-gap narrowing (BGN) at high dopant levels. Without a concise model for BGN in py it is difficult to predict all micro-junction locations from elemental maps. The most likely zones for junctions however, would be regions with high spatial gradients, notably the smaller satellite cubic and euhedral crystals surrounding the two grains as well as regions in the large grains displaying high As-Ni variation.

Thermoelectric and four point resistivity (co-linear or Van de Pauw) measurements could not be carried out to confirm the above predictions due to: (A) concern that impurities on metallic probes will contaminate electron probe and LBIC measurements and (B) that any measurements would be highly erratic and acutely dependent on probe locations as inferred from the measured impurity distributions. However, LBIC measurements to be discussed confirm both grains to be largely *p*-type. With respect to resistivity, Pridmore et al. (Pridmore 1976) and Savage et al. (Savage 2008) have noted resistivity measurements in natural samples to be dubious without recourse to detailed knowledge on local structure, particularly the presence of cracks and large heterogeneities such as the As zones noted here. No attempt was made here.

Besides high spatial gradients in extrinsic doping, heterojunctions also form between mixed sulfide phases as mentioned in the introduction. Within the main grains there exist numerous inclusions of cp and sp, most being less than 5-10 μm in diameter except the large 50 μm sized cp inclusion in the R_2 region close to the middle of the HAGB. Chalcopyrite itself is nearly always an *n*-type semiconductor with a 0.6 eV bandgap between the Cu 3d (valence) and S 3p orbitals (valence) and the Fe 3d orbitals (conduction) (Crundwell 1988). The sp inclusions being less frequent are also smaller; it has a wide bandgap of either 3.54 eV or 3.91 eV at 300 K depending on its structure and can be either *n* or *p*-type depending on stoichiometry. The wurzite structure (3.54eV) is expected to be *n*-type whereas the sphaelarite structure (3.91eV) is *p*-type (Pearce 2006). In theory we expect it to also form heterojunctions. However, its wide-band gap means no free carriers are generated by the visible LBIC laser within these inclusions. Any LBIC signal will be severely reduced or even below detection except at the heterojunction edge. Sampling at 20 μm steps to cover the entire sample means missing that sharp transition is possible.

Maps of Micro-junctions

Consider the series of maps shown in **Figure 5**. Two large lobe-like structures can be seen centered around each electrode in the low-frequency $|P|$ map on the far left. The probes themselves can be seen by their shadow as marked on the 20 Hz map. These lobes are an unwanted artifact due to the thermal gradient between the two remote probes. Interestingly however, the sign of the thermal artifact can be used to confirm conductivity type as follows. When the laser is scanning close to a particular electrode, say the top right probe in **Figure 5** its local temperature increases with respect to the left probe resulting in a thermoelectric current via the Seebeck effect. The total current measured P is therefore the sum of the LBIC photocurrent P_{LBIC} and a thermoelectric contribution P_{TE} i.e. $P = P_{LBIC} + P_{TE}$. Close to each electrode $P \cong P_{TE}$ and its polarity measured by the LIA gives the semiconductor type. In this case the sign inferred from the 20Hz map in **Figure 5** confirms *overall* *p*-type pyrite for both grains as predicted by the elemental maps.

As modulation increases however, the thermal artifact contracts rapidly towards each electrode. As detailed in Appendix 1 in the Supplementary Material, the LBIC intensity modulation-dependent dispersion relationship can be used to discriminate areas dominated by the artifact. These areas are largely centered on each probe and decrease in extent at higher frequencies as seen in in **Figure 5**. For reasons discussed in the appendix, the 500 Hz dataset is to 1st order free of thermoelectric contribution except for a small remnant presence at each electrode tip. The complete phasor dataset for 500 Hz including the phase map ϕ is shown in Error! Reference source not found. in the Appendix. Importantly, the 500Hz data set exhibits several highly contrasted junctions within the thermoelectric free zone towards the middle of the HAGB. By comparison to the elemental maps we can verify that these are spatially correlated with cp-py interfaces and hence electrical heterojunctions with the energy-band diagram given in **Figure 1**(B).

The general peak and trough behavior throughout the remainder of the grains is related to considerably weaker field distributions with complex interplay acting over broad regions of the sample. Remember that each unitary field source displays a peak, trough and peak in $|P|$. Undulations like these are most probably due to band shifting related to BGN from high levels of As, Ni and defect densities near small fractures etc. It is even possible that some may be induced via free charge being trapped at deep levels during the LBIC measurement. The surface inversion or double layer noted by Bronold et al. due to *d*-metal symmetry reduction and lower co-ordination only acts over a few atomic layers in freshly cleaved pyrite (Bronold et al. 1994). The surface in this case would be well passivated by oxide growth. Even for an etched or cleaved surface where the field can be quite high, any LBIC signal would be well below the minimum detection limit since an extremely short diffusion length means almost no minority carriers (electrons in this case) would make it to the surface.

Regions electrically isolated from the dual grains are unlikely to be observed as they present a series resistance R_n or R_p greater than the dynamic resistance R_j of any micro-junction present therein i.e. the excess charge generated in any junction would simply recombine across the local junction and not escape via a lateral current. This is in fact born out in the LBIC data as no additional grains were noted beyond a small reflection based trace from the small square euhedral pyrite grain. The hyper-probe data does in fact confirm the surrounding material to be altered quartz, largely an insulator (online resource).

Unlike the large py-cp junction in the R_2 region, other smaller groupings of cp inclusions such as those in R_1, R_3 and R_4 do not appear to contain resolvable micro-junctions. This may appear odd but these inclusions are either (A) too small for the LBIC scan to resolve or (B) contain high levels of metals like Ag that may short the junction. The R_1 region for example, contains higher than 1000ppm Ag according to electron-probe data (online resource). With respect to (A) the minority carrier diffusion length is extremely short in these minerals so anything but a direct shot at the edge will not cause a response.

IMPLICATIONS

Micro-junctions within and between sulfide phases have important implications for a wide variety of diagenetic mineral processes including oxidation, preferential dissolution and re-crystallization as well as galvanic effects [A] leading to ore deposition by metal reduction from contacting fluids within the right pH range and metallic concentration via gettering and Oswald ripening [B]. This last point is speculation based on similar processes occurring in industrial processing of semiconductors. Specific points related to these implications are summarized below:

A. Impurity heterogeneity and its influence on electrical properties will partly control lithification of pyrite into massive sulfide ores and is key to the resultant mineralization textures including the partitioning of elements such as gold co-transported by the initial magma (Rickard 2012). Crystallization processes are well known to depend on Fermi level positions since these dictate the availability or otherwise of free electrons to partake in bond formation at the front. Impurities can impede or enhance rates of crystallization and alter interaction with other phases once contacted. Similar concepts can be applied to weathering processes.

B. Although the ultimate focus of this research has been better understanding micro-galvanic adsorption of gold onto sulfides (Moller and Kersten 1994, Sakharova et al. 1975) and unraveling potential vectors for exploration, it is worth noting that *p*-*n* junctions are likely to cause the precipitation of a broad range of base and precious metals. This micro-galvanic deposition relies on electrical shorting of the two nodes of the *p*-*n* junction that drives the circuit into forward bias with electrons traveling across the junction from the *n*-anode via its dissolution. The electron current appearing on the *p*-cathode side re-fills surface states as they lose electrons via a tunneling process across the Helmholtz layer to the redox state in question (Crundwell 1988). The properties of the surface and junction (including its OCV) ultimately control the rate of flow of carriers. Since the range of surface conditions able to accommodate this process may be narrow, fracture via tectonic activity coupled with an injection of fluid containing metallic ions may be a precursor for this diagenetic mode. Importantly this trap can operate in solutions well undersaturated with respect to the metal ion in question and over a wide range of temperatures. These issues will be explored later.

C. Another intriguing possibility is that the potential distributions present in and close to these junctions may enhance or retard thermally controlled diffusion process for mobile ions depending on their charge state and position with respect to the junction in question. Since the As side of any pyrite junction is *p*-type, any field distribution will have vector components pointing towards it. Positively charged mobile ions such as Au^+, not substituted onto lattice locations in neighboring *n*-regions that diffuse to within a Debye length of the As side will be transported across it whilst those already there will see a weak electrostatic barrier opposing diffusion back across, even at hydrothermal temperatures where the ions thermal energy is significantly higher. This process might over time concentrate Au^+ ions along a rim-like zone that could ultimately lead to agglomeration via Otswald ripening into nanoparticulate form to reduce their Gibbs free energy. For example, Neumayr et al.

observed a strong spatial correlation between invisible gold and grain boundaries in a zoned assemblage of Archaen arsenopyrite and loellingite ($FeAs_2$) (Neumayr 1993). As with the cp-py heterojunctions observed here, these boundaries contain *E*-field distributions and associated potential wells that preferentially scavenge trace metals from the solid as well as interacting fluids passing through any porous paths associated with the boundary. Once scavenged they are kept in place due to the potential well/diffusion barrier discussed above.

The ability to locate potential gradients under lightly weathered surfaces using LBIC and correlate them with impurity heterogeneity is an important first step in evaluating what combination of elements and spatial relationships are likely to result in electric field distributions near the surface that may alter fluid redox potentials related to metal ore deposition. Here we have for the first time positively identified electrical micro-junctions related to heterojunctions formed between mixed sulfides (cp and py). Much weaker junctions as measured by their relative field strength are probably related to As-Ni variation. The work presented illustrates the complexity in electrical properties for even relatively simple assemblages. In future work using the same methods we hope to unravel some of the perplexing links between electrical properties and galvanic-mediated diagenetic processes at sulfide surfaces leading to precious metal ore genesis.

Figure Captions

Figure 1: Band edges E_c and E_v as well as their centers of gravity for common metal sulfides including pyrite and chalcopyrite referenced to the vacuum (eV) and SHE (V). Also shown is the energy-band diagram for a micro-junction, in this case a heterojunction between *p*-type FeS_2 and *n*-type CuFeS. A shift in bands is required for E_f^p and E_f^n to align at the interface. In the E-field between x_p and x_c (green dashed lines) any excess electrons and holes move down and up the energy-band diagram, respectively. A single phase micro-junction is similar except that the Fermi levels in the *n* and *p*-regions of the same material need to equilibrate.

Figure 2: Band diagram of pyrite. The dominant acceptor level is As_S and possibly a defect related to the absence of a S atom i.e a vacancy noted S_v also attributed to a donor level by Ares et al. An Fe_v is thought to result in an acceptor level close to the VB. Co and Cu on the other hand are donor levels close to the conduction band edge. Ni is a deep level close to mid-gap and has no role in determining bulk carrier concentration via doping. It does however have a large role in determining generation recombination currents.

Figure 3: (Top) Equivalent electrical circuit for a metallurgically clean boundary between *n* and *p*-type pyrite, or similarly, a hetero-junction between two mixed sulfide phases such as pyrite and chalcopyrite. (Bottom) The bipolar remote LBIC signal P (f_m) measured across the junction $-x_n$ to x_p as the modulated laser S (f_m) is scanned from left to right including an inherent phase ϕ due to the effective circuit as seen by external electronics. Also shown is the charge stored on the depletion edge constituting a capacitance, C_j. A zero signal or trough exists at the weighted average center of the junction. Sub-micron minority carrier diffusion lengths L_p and L_n dictate the lateral extent of the imaged junction in the *n* and *p*-type regions, respectively.

Figure 4: (TOP) A BSE image of the arsenian pyrite under analysis in this study. The central euhedral grains are predominantly pyrite (orange) with small inclusions of cp, sp, rutile and

carbonates. Both grains are surrounded by heavily altered quartz and sp dispersed in shale (grey). A HAGB between the two large euhedral py grains is marked B-B'. Images of Co, Ni and As are also shown as an RGB map. Maximum values for As, Ni and Co are 2.7, 1.0 and 0.8 wt%, respectively. Cu levels in the py are extremely low and most Cu exists locked in as micro-inclusions of cp marked R_1 to R_4. The lower level of the Cu map has been artificially limited to 1% to make the pyrite matrix visible. Several cp grains can also be seen outside the pyrite complex. (BOTTOM) Effective extrinsic doping map $D(x,y)$ for the Otago sample is primarily dictated by the difference in As (*p*-type) and Co (*n*-type) impurities. Although large spatial gradients exist throughout the entire field of view at no position does D go negative indicating overall *p*-type behavior in the pyrite.

Figure 5: A series of LBIC images (X,Y and $|P|$) versus modulation frequency from 20 to 500 Hz. A higher f_m dramatically reduces thermal artifacts near each electrode. The rectangular area marked on the 20Hz $|P|$ map encompasses the large chalcopyrite inclusions along the HAGB. Unlike the lobe regions close to each electrode, its response remains high independent of frequency. LBIC-X profile through the R_2 zone displays a negative to positive transition over the py-cp-py transition that agrees with that expected for a heterojunction. Also shown is the Cu elemental map covering the same transect. Note the ~25°angle between the Cu and LBIC-X maps.

REFERENCES

Abraitis, P. K., Pattrick, R. A. D. and Vaughan, D. J. (2004) Variations in the compositional, textural and electrical properties of natural pyrite: a review. *International Journal of Mineral Processing* **74,** 41–59

Altermatt, P. P., Kiesewetter, T., Ellmer, K. and Tributsch, H. (2002) Specifying targets of future research in photovoltaic devices containing pyrite (FeS2) by numerical modelling. *Solar Energy Materials and Solar Cells* **71,** 181–195

A M Karguppikar, (1988) Electrical and optical properties of natural iron pyrite (FeS2). **109,** 549–558

Ares, J. R., Pascual, A., Ferrer, I. J. and Sanchez, C. R. (2004) Lattice intrinsic defects and electrical resistivity in pyrite thin films. *Thin Solid Films* **451,** 233–236

Bajaj, J., Tennant, W. E., Zucca, R. and Irvine, S. J. C. (1993) SPATIALLY-RESOLVED CHARACTERIZATION OF HGCDTE MATERIALS AND DEVICES BY SCANNING LASER MICROSCOPY. *Semiconductor Science and Technology* **8,** 872–887

Becker, U., Rosso K.M., and Hochella, M.F. (2001) The proximity effect on semiconducting mineral surfaces: A new aspect of mineral surface reactivity and surface complexation theory ? *Geochimica et Cosmochimica Acta* 65(16), 2641-2649

Besten, den, J., Jamieson, D. N. and Ryan, C. G. (1999) Lattice location of gold in natural pyrite crystals. *Nuclear Instruments and Methods in Physics Research: Section B-Beam Interaction With Matter and Atoms,* 1–10

Bither, T. A., Bouchard, R. J., Cloud, W. H., Donohue, P. C. and Siemons, W. J. (1968) TRANSITION METAL PYRITE DICHALCOGENIDES HIGH-PRESSURE SYNTHESIS AND CORRELATION OF PROPERTIES. *Inorganic Chemistry* **7,** 2208

Breese, M. B. H., King, P. J. C., Grime, G. W. and Watt, F. (1992) Microcircuit imaging using an ion-beam-induced charge. *Journal of Applied Physics* **72,** 2097

Bronold, M., Buker, K., Kubala, S., Pettenkofer, C. and Tributsch, H. (1993) SURFACE PREPARATION OF FES2 VIA ELECTROCHEMICAL ETCHING AND INTERFACE FORMATION WITH METALS. *Phys. Status Solidi A-Appl. Res.* **135,** 231–243

Bronold, M., Tomm, Y. and Jaegermann, W. (1994) SURFACE-STATES ON CUBIC D-BAND SEMICONDUCTOR PYRITE (FES(2)). *Surface Science* **314,** L931–L936

Buchner, S., Knudson, A., Kang, K. and Campbell, A. B. (1988) Charge collection from focussed picosecond laser pulses. *Nuclear Science, IEEE Transactions on* **35,** 1517–1522

Buker, K., Alonso Vante, N. and Tributsch, H. (1992) Photovoltaic output limitation of n-FeS2 (pyrite) Schottky barriers: A temperature-dependent characterization. *Journal of Applied Physics* **72,** 5721–5728

Chandra, A. P. and Gerson, A. R. (2010) The mechanisms of pyrite oxidation and leaching: A fundamental perspective. *Surface Science Reports* **65,** 293–315

Chandler, R. N. & Bené, R. W. EPR Study of FeS2: Ni,Co (1974) *American Institute of Physics Conference Series* **18,** 534–534

Craig, J. R., Vokes, F. M. and Solberg, T. N. (1998) Pyrite: physical and chemical textures. *Mineralum. Deposita.* **34,** 82–101

Crundwell, F. K. (1988) The influence of the electronic structure of solids on the anodic dissolution and leaching of semiconducting sulphide minerals. *Hydrometallurgy* **21,** 155–190

Dasbach, R. (1994) PhD Thesis, Basic investigations on Pyrite thin-film solar cells. (University of Konstanz).

Doyle, F. M. and Mirza, A. H. (1996) Electrochemical oxidation of pyrite samples with known composition and electrical properties. *Proceedings of the Fourth International Symposium on Electrochemistry in Mineral and Metal Processing* **96,** 203–214

Ennaoui, A. and Tributsch, H. (1986) ENERGETIC CHARACTERIZATION OF THE PHOTOACTIVE FES2 (PYRITE) INTERFACE. *Solar Energy*

Materials **14,** 461–474

Ennaoui, A. *et al.* (1993) IRON DISULFIDE FOR SOLAR-ENERGY CONVERSION. *Solar Energy Materials* **29,** 289–370 (1993).

Ennaoui, A., Fiechter, S., Goslowsky, H. and Tributsch, H. (1985) PHOTOACTIVE SYNTHETIC POLYCRYSTALLINE PYRITE (FES2). *Journal of the Electrochemical Society* **132,** 1579–1582

Fleet, M. E., Chryssoulis, S. L., Davidson, R., Weisener, C. G. and Maclean, P. J. (1993) Arsenian pyrite from gold deposits: Au and As distribution investigated by SIMS and EMP, and color staining and surface oxidation by XPS and LIMS. *Canadian Mineralogist* **31,** 1–17

Fleet, M. E. and Mumin, A. H. (1997) Gold-bearing arsenian pyrite and marcasite and arsenopyrite from Carlin Trend gold deposits and laboratory synthesis. *American Mineralogist* **82,** 182–193

Fynn, K. A., Bajaj, J. & Faraone, L. A (1995) DISCRETE ELEMENT MODEL OF LASER-BEAM INDUCED CURRENT (LBIC) DUE TO THE LATERAL PHOTOVOLTAIC EFFECT IN OPEN-CIRCUIT HGCDTE PHOTODIODES. *Electron Devices, IEEE Transactions on* **42,** 1775–1782

Ho, C. H., Huang, Y. S. and Tiong, K. K. (2006) Characterization of near band-edge properties of synthetic p-FeS2 iron pyrite from electrical and photoconductivity measurements. *Journal of Alloys and Compounds* **422,** 321–327

Huang, Y.S., Huang, J.K and Tsay M.Y (1993) An electrolyte electro-reflectance study of FeS2, Journal of Physics: Condensed Matter, 5 7827

Kou, W. W. and Seehra, M. S. (1978) Optical-Absorption in Iron Pyrite (Fes2). *Physics Review B* **18,** 7062–7068 (1978)

Laird, J. S., Johnson, B. C. and Ryan, C. G. (2012) Laser-beam-induced current microscopy of electric fields in natural minerals caused by impurity zonation and structural defects. *Measurement Science and Technology* **23,** 085401

Large, R. R. *et al.* (2009) Gold and Trace Element Zonation in Pyrite Using a Laser Imaging Technique: Implications for the Timing of Gold in Orogenic and Carlin-Style Sediment-Hosted Deposits. *Economic Geology* **104,** 635–668

Leamy, H. J. (1982) Charge collection scanning electron microscopy. *Journal of Applied Physics* **53,** R51

Lehner, S. W., Savage, K. S. and Ayers, J. C. (2006) Vapor growth and characterization of pyrite (FeS2) doped with Co, Ni, and As: Variations in semiconducting properties. *Journal of Crystal Growth* **286,** 306–317 (2006)

Lehner, S., Savage, K., Ciobanu, M. and Cliffel, D. E. (2007) The effect of As, Co, and Ni impurities on pyrite oxidation kinetics: An electrochemical study of synthetic pyrite. Geochimica et Cosmochimica Acta **71,** 2491–2509

Lehner, S. W. *et al.* (2012) Defect energy levels and electronic behavior of Ni, Co, and As-doped synthetic pyrite (FeS2). *Journal of Applied Physics* **111**

Li, Y. Q., Chen, J. H., Chen, Y. and Guo, J. (2011) Density functional theory study of influence of impurity on electronic properties and reactivity of pyrite. *Transactions on Nonferrous Metals Society of China* **21,** 1887–1895

Macrae, C. M., Wilson, N. C., Johnson, S. A., Phillips, P. L. and Otsuki, M. (2005) Hyperspectral mapping—combining cathodoluminescence and X-ray collection in an electron microprobe. *Microsc. Res. Tech.* **67,** 271–277

Maddox, L. M., Bancroft, G. M., Scaini, M. J. and Lorimer, J. W. (1998) Invisible gold: Comparison of Au deposition on pyrite and arsenopyrite. *American Mineralogist.* **83,** 1240–1245 (1998).

Marion, P., Holliger, P., Boiron, M. C., Cathelineau, M. and Wagner, F. E. (1991) NEW IMPROVEMENTS IN THE CHARACTERIZATION OF REFRACTORY GOLD IN PYRITES - AN ELECTRON-MICROPROBE, MOSSBAUER SPECTROMETRY AND ION MICROPROBE STUDY. *Brazil Gold 91: the Economics, Geology, Geochemistry and Genesis of Gold Deposits* 389–395

Melinger, J. S. *et al.* (1994) Critical Evaluation of the Pulsed Laser Methods for Single Event Effects Testing and Fundamental Studies. *IEEE Transactions on Nuclear Science,* **41,** 2574–2584

Moller, P and Kersten, G (1994) Electrochemical Accumulation of Visible Gold on Pyrite and Arsenopyrite Surfaces, Mineral Deposita 29, 404-413

Neumayr, P., Cabri, L. J., Groves, D. I., Mikucki, E. J. and Jackman, J. A. (1993) The mineralogical distribution of gold and relative timing of gold mineralization in two Archean settings of high metamorphic grade in Australia. *The Canadian Mineralogist* **31,** 711–725

Niu, H., Matsuda, T., Yamauchi, K. and Takai, M. (1972) Lateral photovoltaic effect in nitrogen-implanted p-type silicon. *Appl. Phys. Lett.* **21,** 423–424

Niu, H., Matsuda, T., Sadamatsu, H. and Takai, M. (1976) Application of Lateral Photovoltaic Effect to the Measurement of the Physical Quantities of P- NJunctions–Sheet Resistivity and Junction Conductance of N 2+Implanted Si. *Japanese Journal of Applied Physics* **15,** 601–609 (1976).

Niu, H., Metsuda, T., Okada, S. and Takai, M (1977) DYNAMIC CHARACTERISTICS OF THE LATERAL PHOTOVOLTAIC EFFECT AND THEIR APPLICATION TO THE MEASUREMENT OF JUNCTION CAPACITANCE. *Jpn J Appl Phys* **16,** 1589–1599 (1977).

Pearce, C. I. (2006) Electrical and Magnetic Properties of Sulfides. *Reviews in Mineralogy and Geochemistry* **61,** 127–180 (2006).

Pridmore, D. F. and Shuey, R. T. (1975) GEOCHEMICAL CONTROL OF CONDUCTIVITY AND TYPE IN GALENA, PYRITE, AND CHALCOPYRITE. *Geophysics* **40,** 153–154

Pridmore, D. F. and Shuey, R. T. (1976) ELECTRICAL-RESISTIVITY OF GALENA, PYRITE, AND CHALCOPYRITE. *American Mineralogist.* **61,** 248–259

Redfern, D.A PhD thesis (2004) University of Western Australia, Australia.

Redfern, D. A., Smith, E. P. G., Musca, C. A., Dell, J. M. and Faraone, L. (2006) Interpretation of current flow in photodiode structures using laser beam-induced current for characterization and diagnostics. *Electron Devices, IEEE Transactions on* **53,** 23–31

Rickard, D (2012)

M.S. Sakharova, Y.A. Batrakova, and S.K. Ryakhovskaya, Geokhimiya 740 (1975).

Schieck, R., Hartmann, A., Fiechter, S., Konenkamp, R. and Wetzel, H. (1990) ELECTRICAL-PROPERTIES OF NATURAL AND SYNTHETIC PYRITE (FES2) CRYSTALS. *J. Mater. Res.* **5,** 1567–1572

Savage, K. S., Stefan, D. and Lehner, S. W. (2008) Impurities and heterogeneity in pyrite: Influences on electrical properties and oxidation products. *Applied Geochemistry* **23,** 103–120

Sze, S. M. Physics of Semiconductor Devices 1st Edition (1985). (John Wiley and Sons).

Tributsch, H., Fiechter, S., Jokisch, D., Rojas-Chapana, J. and Ellmer, K. (2003) Photoelectrochemical power, chemical energy and catalytic activity for organic evolution on natural pyrite interfaces. *Orig. Life Evol. Biosph.* **33,** 129–162

Vaughan, D. J. and Lennie, A. R. (1991) THE IRON SULFIDE MINERALS - THEIR CHEMISTRY AND ROLE IN NATURE. *Science Progress* **75,** 371–388

Yu, J.T., Wu, C.J., Huang, Y.S. and Lin, S.S. (1992) Electron-paramagnetic-resonance study of the Cr^{3+} and Ni^{2+} ions and the $(SCl)^{2-}$ defect in FeS_2. *Journal of Applied Physics* **71,** 370

Zhang, H., Zhang, R., Wan, D., Wang, B. and Wei, L. Effects of doping impurites in pyrite films on the optical and electric properties. *Taiyangneng Xuebao/Acta Energiae Solaris Sinica* **27,** 423–427 (2006).

Zhao, G. L., Callaway, J. and Hayashibara, M. (1993) Electronic-Structures of Iron and Cobalt Pyrites. *Physics Review B* **48,** 15781–15786 (1993).

FIGURES

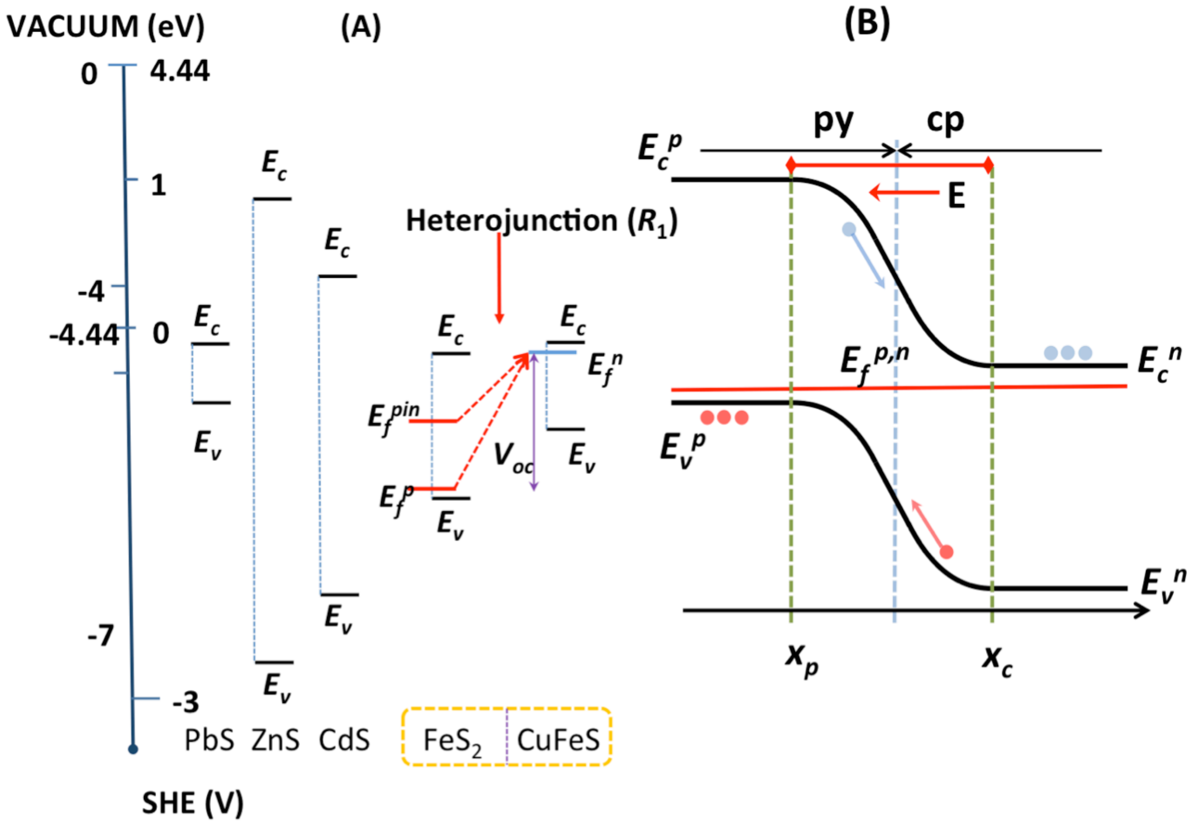

Figure 1:

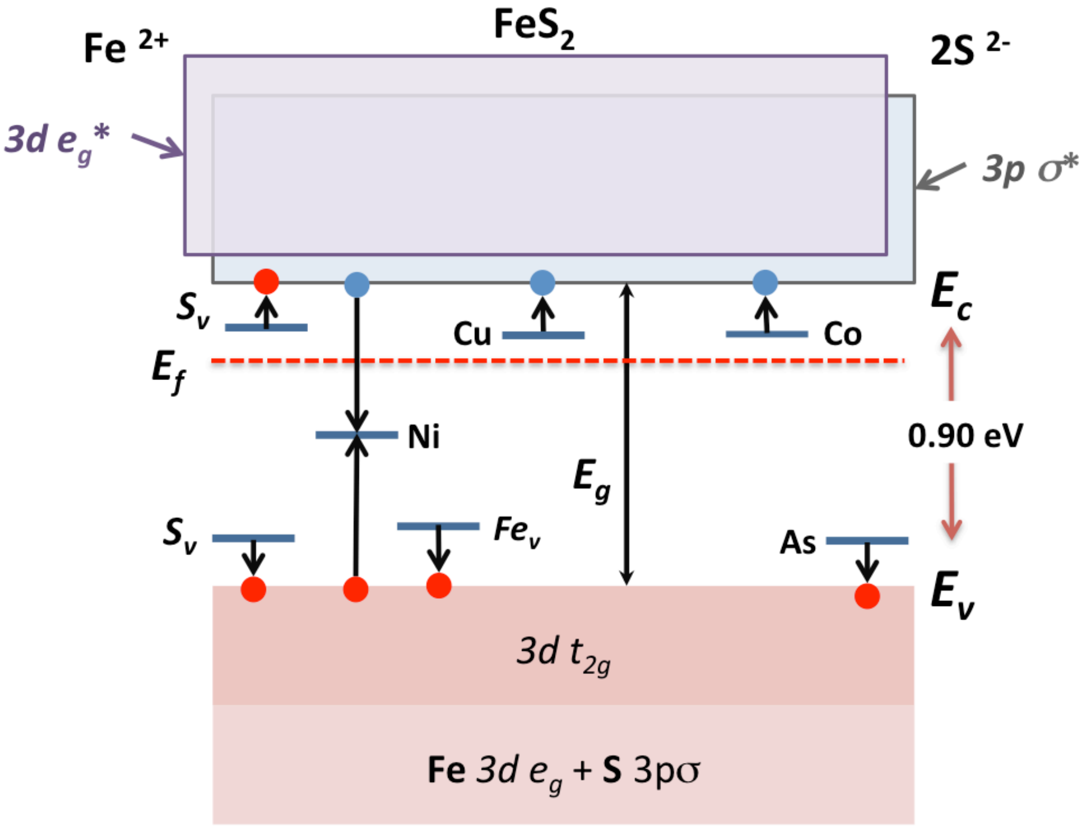
FeS$_2$
Fe $^{2+}$
2S $^{2-}$
3d e_g*
3p σ*
E_c
S_v
Cu
Co
E_f
Ni
0.90 eV
E_g
S_v
Fe_v
As
E_v
3d t_{2g}
Fe 3d e_g + S 3pσ

Figure 2

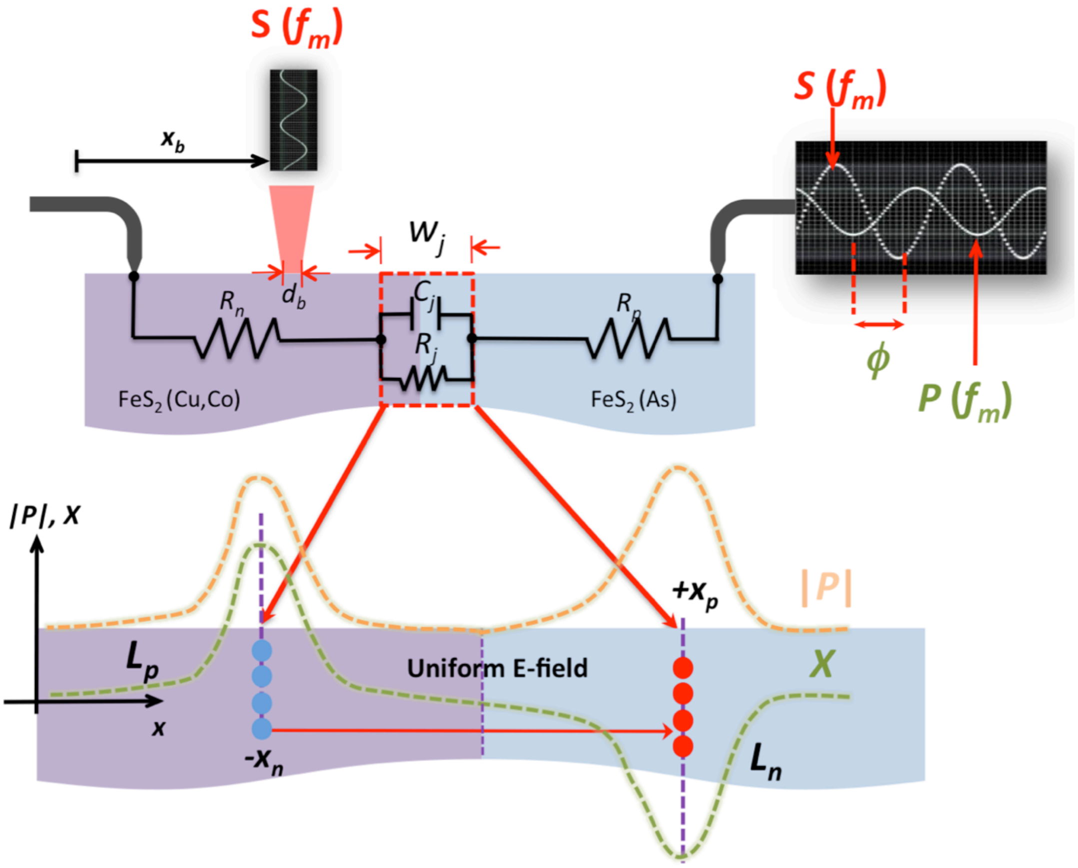
S (f_m)
x_b
S (f_m)
W_j
d_b
C_j
R_n
R_j
R_p
FeS_2 (Cu,Co)
FeS_2 (As)
ϕ
P (f_m)
|P|, X
+x_p
|P|
L_p
Uniform E-field
X
x
-x_n
L_n

Figure 3:

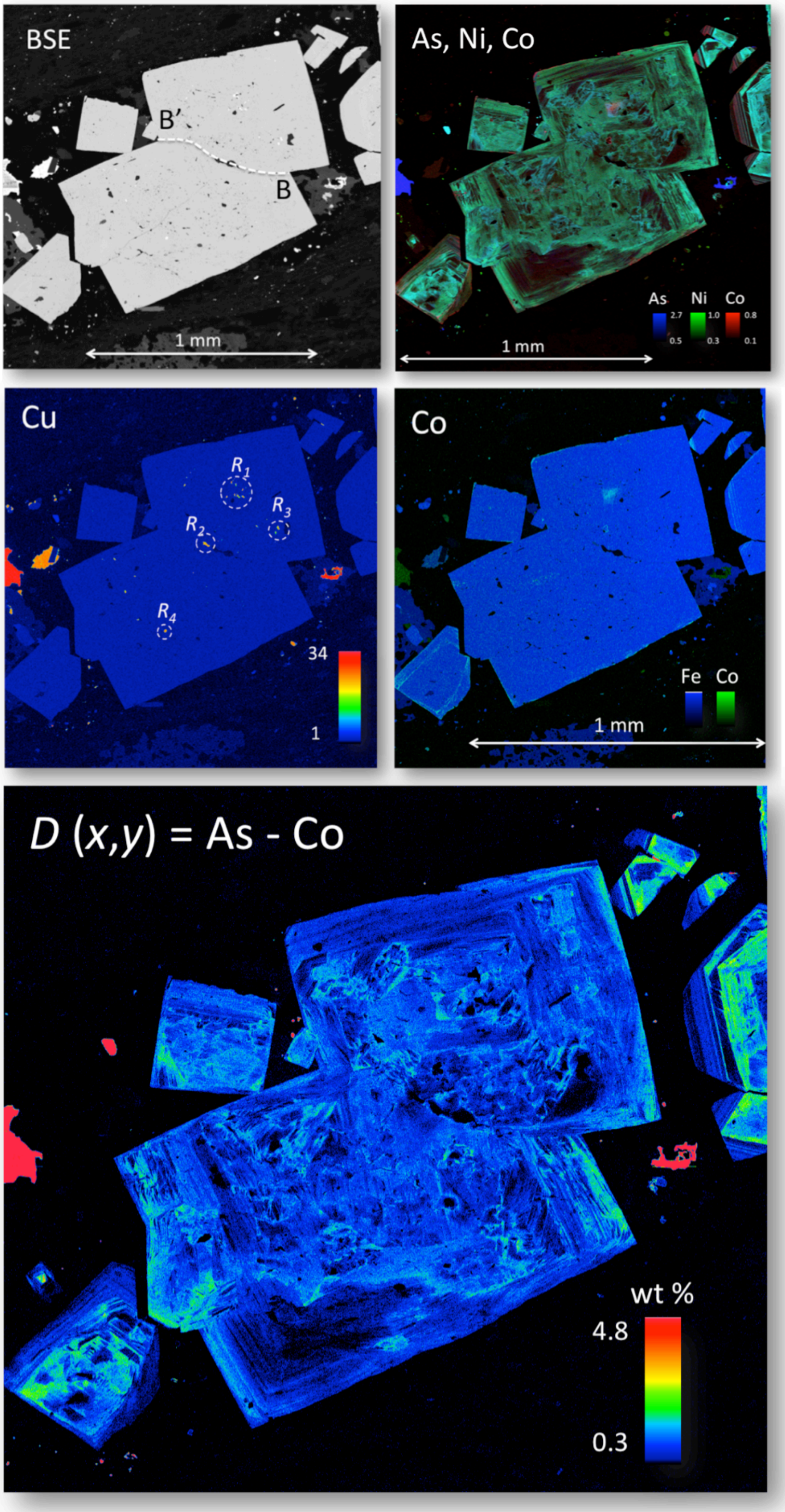
BSE
B'
B
1 mm
As, Ni, Co
As
Ni
Co
2.7
0.5
1.0
0.3
0.8
0.1
1 mm
Cu
R1
R2
R3
R4
34
1
Co
Fe
Co
1 mm
D (x,y) = As - Co
wt %
4.8
0.3

Figure 4:

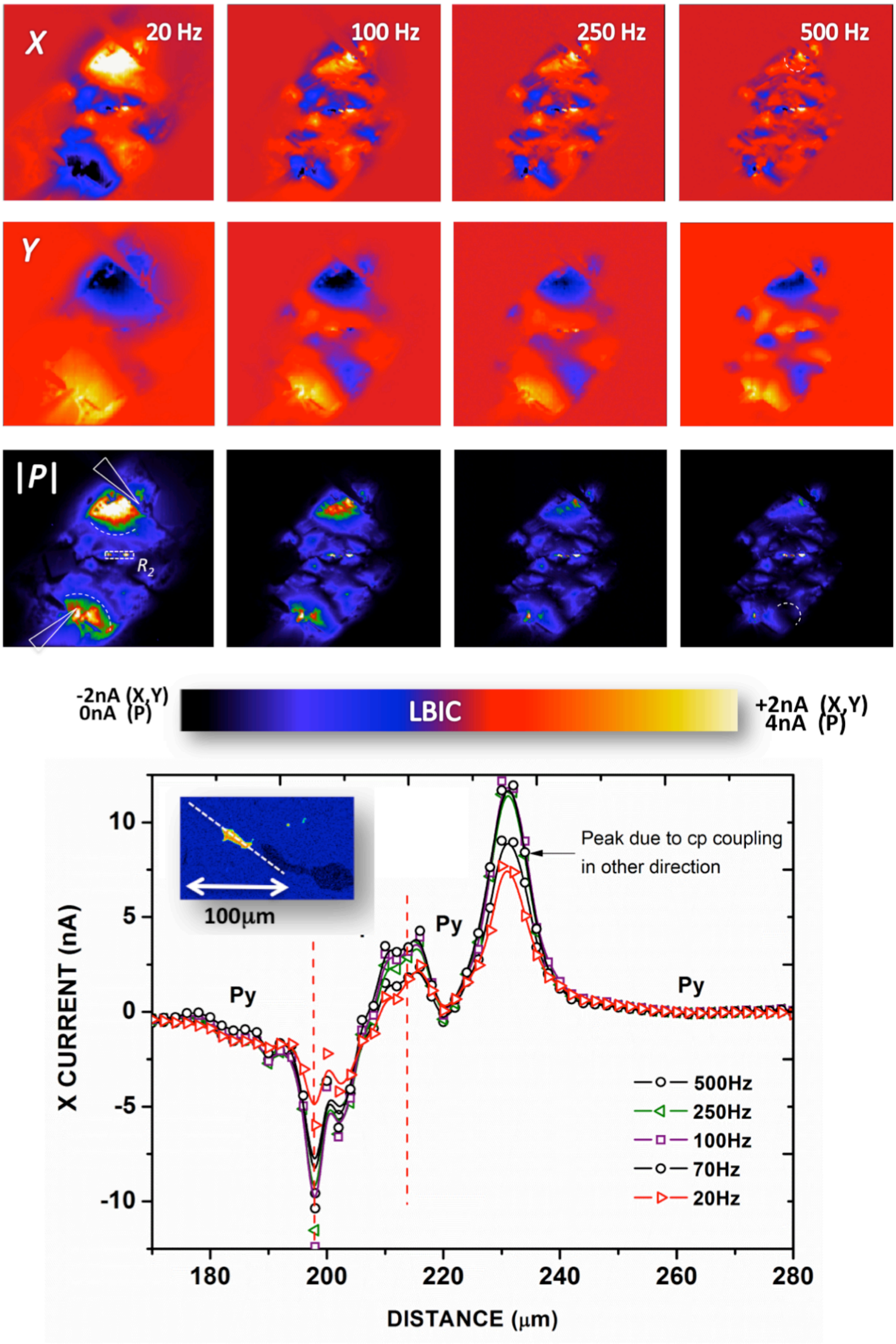
X
20 Hz
100 Hz
250 Hz
500 Hz
Y
|P|
R2
-2nA (X,Y)
0nA (P)
LBIC
+2nA (X,Y)
4nA (P)
100μm
Peak due to cp coupling in other direction
Py
Py
Py
X CURRENT (nA)
10
5
0
-5
-10
180
200
220
240
260
280
DISTANCE (μm)
500Hz
250Hz
100Hz
70Hz
20Hz

Figure 5: